GEOPHYSICS, VOL. 71, NO. 3 (MAY-JUNE 2006); P. H33–H44, 15 FIGS., 4 TABLES.
10.1190/1.2192927

Integration of diverse physical-property models: Subsurface zonation and petrophysical parameter estimation based on fuzzy *c*-means cluster analyses

Hendrik Paasche[1], Jens Tronicke[1], Klaus Holliger[2], Alan G. Green[3], and Hansruedi Maurer[3]

ABSTRACT

Inversions of an individual geophysical data set can be highly nonunique, and it is generally difficult to determine petrophysical parameters from geophysical data. We show that both issues can be addressed by adopting a statistical multiparameter approach that requires the acquisition, processing, and separate inversion of two or more types of geophysical data. To combine information contained in the physical-property models that result from inverting the individual data sets and to estimate the spatial distribution of petrophysical parameters in regions where they are known at only a few locations, we demonstrate the potential of the fuzzy *c*-means (FCM) clustering technique. After testing this new approach on synthetic data, we apply it to limited crosshole georadar, crosshole seismic, gamma-log, and slug-test data acquired within a shallow alluvial aquifer. The derived multiparameter model effectively outlines the major sedimentary units observed in numerous boreholes and provides plausible estimates for the spatial distributions of gamma-ray emitters and hydraulic conductivity.

INTRODUCTION

Multiparameter approaches can significantly reduce uncertainties in geophysical data analysis and interpretation (Dannowski and Yaramanci, 1999; Tronicke et al., 1999; Hubbard et al., 2001; Garambois et al., 2002; Yaramanci et al., 2002; Aaltonen, 2003; Gaffney et al., 2004; Kostyuchenko et al., 2004; Tronicke et al., 2004). The most common approach of jointly interpreting independent physical-property models derived from different types of coincident geophysical data is largely qualitative in nature, such that the outcome depends greatly on the experience and preconceptions of the interpreter and there is no objective way of assessing the internal consistency of the interpretation.

More quantitative approaches require linking different geophysical data sets during the model-generation process (Vozoff and Jupp, 1975). By jointly inverting multiple data sets, all available information is used to constrain models that explain the individual data sets, thus markedly decreasing the inherent ambiguities associated with geophysical model derivation. A disadvantage of joint inversions is the need to assume well-defined relationships between the various parameters (Gallardo and Meju, 2003; Musil et al., 2003; Bosch, 2004). The quality and consistency of multiparameter models depend critically on the reliability of these assumptions and the way they are implemented in the inversion procedure. Unfortunately, such parameter relationships tend to be nonunique and site specific (Schön, 1998). Nevertheless, ongoing algorithmic and computational improvements are expected to enhance the appeal and applicability of joint inversion schemes.

A fundamentally different approach to model integration involves the application of multivariate statistics. Clustering methods (Kaufmann and Rousseeuw, 1990; Höppner et al., 1999) that do not require prior knowledge about the specific interrelationships of the various parameters have been used for this purpose. Hard clustering methods (e.g., the *k*-means technique) attribute each point in the multidimensional parameter space to a single cluster (Dietrich et al., 1998; Tronicke et al., 2004). By comparison, soft clustering methods (e.g., the fuzzy *c*-means technique) distribute the influence of each point among several clusters. Applications of fuzzy *c*-means (FCM) clustering in the geosciences include soil classification (De Bruin and Stein, 1998; Bragato, 2004), analysis

Manuscript received by the Editor April 5, 2005; revised manuscript received November 10, 2005; published online June 6, 2006.
[1]University of Potsdam, Department of Geosciences, P. O. Box 601553, D-14415 Potsdam, Germany; formerly Swiss Federal Institute of Technology (ETH). E-mail: hendrik@geo.uni-potsdam.de; jens@geo.uni-potsdam.de.
[2]Formerly Swiss Federal Institute of Technology (ETH); presently University of Lausanne, Institute of Geophysics, CH-1015 Lausanne, Switzerland. E-mail: klaus.holliger@unil.ch.
[3]Swiss Federal Institute of Technology (ETH), Institute of Geophysics, ETH Hönggerberg, CH-8093 Zurich, Switzerland. E-mail: alan@aug.ig.erdw.ethz.ch; maurer@aug.ig.erdw.ethz.ch.

of geochemical and rock magnetic parameters in different materials (Kruiver et al., 1999; Urbat et al., 2000; Knab et al., 2001), and the determination of hydrochemical facies distribution in groundwater systems (Güler and Thyne, 2004). Whereas the advantages and disadvantages of hard clustering techniques for geophysical model integration are extensively explored, the potential and limitations of soft clustering methods are largely unknown.

In addition to determining physical-property models from the different geophysical data sets, it is often necessary to use the same data for estimating the distribution of various petrophysical parameters (e.g., lithologies, porosities, and hydraulic conductivities). This is usually achieved by linking the petrophysical parameters to the geophysical data via explicit theoretical and/or empirical expressions (Greaves et al., 1996; Dannowski and Yaramanci, 1999; Garambois et al., 2002). Again, statistical techniques offer alternative approaches. Based on the geophysical data, the distribution of petrophysical parameters can be extrapolated or interpolated over large regions from locations where they are well known (e.g., along boreholes). As examples, Chen et al. (2001) and Hubbard et al. (2001) use a Bayesian approach to interpolate hydraulic conductivities between boreholes using crosshole georadar and seismic data, and Tronicke and Holliger (2005) estimate porosities using conditional simulations of hydrogeophysical data.

In this study, we present a unified approach to physical-property model integration and estimation of the spatial distribution of petrophysical parameters based on FCM cluster analyses. After explaining key aspects of the FCM clustering technique, we briefly describe our geophysical forward-modeling and inversion schemes. Our FCM technique is then tested on synthetic geophysical data generated for a heterogeneous alluvial aquifer model. Finally, the FCM technique is applied to a data set acquired at a hydrological test site in western Switzerland.

METHODOLOGY

In the following, after introducing the basic concepts of the FCM clustering technique and its application to estimating petrophysical parameters, we describe our synthetic porosity model, forward modelling method, and first-break picking and inversion schemes.

FCM cluster analysis

Each node in an integrated subsurface model is characterized by a multiparameter data point defined by the various parameters contained in the individual models. For example, in our synthetic and field examples, each data point has a georadar velocity, a georadar attenuation, and a seismic velocity. Cluster analysis algorithms involve grouping data located in the multidimensional parameter space into a specified number of characteristic subsets or clusters based on their distances to the cluster centers, which are defined by the data sets themselves. In the case of FCM cluster analysis, this is achieved by iteratively minimizing the following objective function (Güler and Thyne, 2004):

$$J_{FCM} = \sum_{i=1}^{c} \sum_{j=1}^{n} md_{ij}^{f} \|x_j - v_i\|^2, \qquad (1)$$

where c is the number of clusters, n is the number of data points, and md_{ij} denotes the degree of membership of data point x_j to cluster i defined by its center v_i. The weighting exponent f [the fuzzification parameter of Güler and Thyne (2004) and Fridgen et al. (2004)] represents the degree of overlap between the clusters. Throughout this study, we use $f = 2$, which is widely accepted as a suitable choice (Hathaway and Bezdek, 2001).

After selecting the number of clusters and randomly defining their initial locations in multiparameter space, iterative minimization of the objective function (equation 1) yields the optimum locations of the cluster centers and the distance of each data point to these centers. To test the validity and robustness of the entire process, we repeat it four times using different initial locations of the cluster centers. For each example presented in this paper, the results of the five independent runs are practically identical.

Data points are assigned partial membership to all clusters based on their distances to the respective cluster centers. The membership values of a data point, which quantify its degrees of membership to the various clusters, vary between zero and one; the higher the membership value, the closer the data point to the corresponding cluster center. For any given data point, the sum of all membership values is unity.

By assigning each data point to the cluster for which it has the highest membership value (defuzzyfication of Melgani et al., 2000), the results of FCM cluster analysis can be converted to equivalent hard cluster models consisting of homogeneous clusters. In our case, the spatial distribution of cluster memberships is a zoned model of the subsurface probed by the various geophysical techniques. The procedure for integrating the various physical-property models is illustrated in Figure 1.

Petrophysical parameter estimation

To use the results of the FCM cluster analyses for estimating the spatial distribution of petrophysical parameters, we require some direct measurements of the target parameters in parts of the investigated subsurface (e.g., as provided by borehole logs or core samples). Based on these measurements, a corresponding mean value of the target petrophysical parameter is assigned to each cluster. Using the previously evaluated membership values md_{ij}

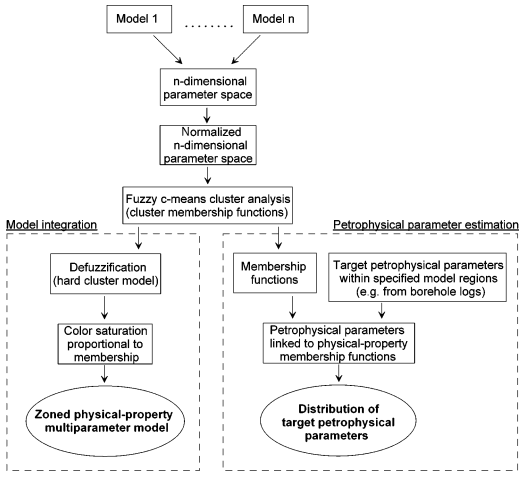

Figure 1. Flowchart illustrating the FCM clustering technique used for physical-property model integration and petrophysical parameter estimation.

(equation 1) as weighting factors, we can estimate the value of the target parameter in the jth grid cell as a weighted sum over all clusters:

$$p_j = \sum_{i=1}^{c} \bar{p}_i \times md_{ij}, \tag{2}$$

where $\bar{p}_i$ is the mean value of the target parameter p for the ith cluster. The corresponding procedure is illustrated in Figure 1. It is conceptually similar to that used for multicomponent petrophysical mixing models (Schön, 1998).

Although there must be a relationship between the physical-property and petrophysical parameters, unlike conventional approaches (Greaves et al., 1996; Dannowski and Yaramanci, 1999; Garambois et al., 2002) the nature of this relationship in FCM cluster analysis can be rather vague and ill defined; it does not need to be explicitly quantified by theoretical or empirical expressions.

Porosity model

We generate a realistic porosity model of a heterogeneous alluvial aquifer using an unconditional stochastic simulation technique (Goff and Jordan, 1988; Tronicke and Holliger, 2005). The porosity distribution is characterized by an exponential autocovariance function and a Gaussian probability density function with a mean of 21% and a standard deviation of 1.1%. These values are typical of alluvial deposits (Gelhar, 1993; Heinz et al., 2003). The exponential autocovariance function is a special case of the versatile band-limited, scale-invariant von Kármán autocovariance model. It is widely used for characterizing heterogeneous anisotropic structures such as alluvial aquifers (Desbarats and Bachu, 1994; Hardy and Beier, 1994). Our model is 20 m long and 10 m deep; it is discretized on a uniform grid with a sample spacing of 0.018 m. To simulate a quasi-layered heterogeneous structure that is scale invariant over the entire range of the model, we use vertical and horizontal correlation lengths of 20 and 100 m, respectively.

We assume complete water saturation and use the following expressions to estimate relative permittivities ε (Wharton et al., 1980), electrical resistivities ρ (Archie, 1942), densities d (Schön, 1998), and P-wave velocities v_P (Raymer et al., 1980) from porosities ϕ:

$$\sqrt{\varepsilon} = \phi \times (\sqrt{\varepsilon_w} - \sqrt{\varepsilon_m}) + \sqrt{\varepsilon_m}, \tag{3}$$

$$\rho = \frac{a}{\phi^b}\rho_w, \tag{4}$$

$$d = (1 - \phi) \times d_m + \phi \times d_w, \tag{5}$$

$$v_P = (1 - \phi)^2 \times v_m + \phi \times v_w, \tag{6}$$

where a and b are empirical parameters and where subscripts w and m refer to water and the dry matrix material, respectively. The values used for the various geophysical parameters (Table 1) are representative of unconsolidated gravely and sandy sediments (Schön, 1998). We use the relative permittivity and resistivity models (equations 3 and 4) as input to generate synthetic crosshole georadar data and the density and P-wave velocity models (equations 5 and 6) as input to generate synthetic crosshole seismic data.

Note that equation 6 was developed initially for sandstones, but for the chosen parameters the resulting velocity range can also be regarded as realistic for unconsolidated clastic sediments (Schön, 1998).

Forward modeling

Full-waveform crosshole georadar data were generated using a staggered-grid, finite-difference time-domain (FDTD) solution of Maxwell's equation in cylindrical coordinates that was second-order accurate in both time and space (Holliger and Bergmann, 2002; Ernst et al., 2006). Transmitters and receivers were modeled as infinitesimal vertical electrical dipoles, a realistic approximation for the radiative behavior of many resistively loaded georadar antennas (Lampe and Holliger, 2005). The source signal was a Ricker wavelet with a dominant frequency of 80 MHz and a bandwidth of 2–3 octaves. It yielded a dominant wavelength of about 1 m and at least 17 gridpoints per minimum wavelength for the 0.018-m grid spacing. At this level of discretization, numerical errors from grid dispersion and grid anisotropy were negligible (Bergmann et al., 1996). The two boreholes extended along the lengths of the model edges. They contained 41 equally spaced transmitter and receiver locations.

The same acquisition geometry was used for the simulation of full-waveform crosshole seismic data after resampling the model to a grid spacing of 0.065 m. We used the ReflexW commercially available software program (Sandmeier Scientific Software, Germany) based on a staggered-grid FDTD solution of the acoustic-wave equation that was second-order accurate in time and fourth-order accurate in space. The source pulse was a Küpper wavelet (Küpper, 1958; Fuchs and Müller, 1971) with a dominant frequency of 600 Hz and a bandwidth of 2–3 octaves. This yielded a dominant wavelength of about 3 m and at least 15 gridpoints per minimum wavelength, which was again adequate for avoiding numerical dispersion and grid anisotropy.

First-break picking and inversion

First arrivals of the synthetic crosshole georadar and seismic data were picked using a semiautomatic picking routine imple-

Table 1. Parameters used in equations 3–6. All values are typical of unconsolidated gravely and sandy sediments (Schön, 1998).

Symbol	Value	Description
ε_w	80	Relative permittivity of pore water
ε_m	4.6	Relative permittivity of dry matrix material
ρ_w	20 Ω.m	Electrical resistivity of pore water
a	0.88	Empirical parameter in Archie's equation
b	1.37	Empirical parameter in Archie's equation
d_m	2.5 g/cm^3	Density of dry matrix material
d_w	1.0 g/cm^3	Density of pore water
v_m	3000 m/s	P-wave velocity of dry matrix material
v_w	1500 m/s	P-wave velocity of pore water

mented in ReflexW. To simulate realistic recording and measuring conditions, Gaussian-distributed random time anomalies with standard deviations of 2 ns and 0.04 ms were added to the picked georadar and seismic traveltimes, respectively (these standard deviations correspond to the estimated picking accuracies of the observed data, discussed later). Maximum first-cycle amplitudes of the direct georadar waves were also measured. The traveltimes were inverted tomographically using an inversion scheme based on a finite-difference solution of the eikonal equation (Lanz et al., 1998) that fully accounted for the curvature of raypaths in heterogeneous media. Our ray-based inversion of georadar amplitude data followed the procedures described by Holliger et al. (2001). The grid spacing used for all tomographic inversions was 0.25 m.

We now combine the various physical-property models and then demonstrate the results of estimating the petrophysical parameters.

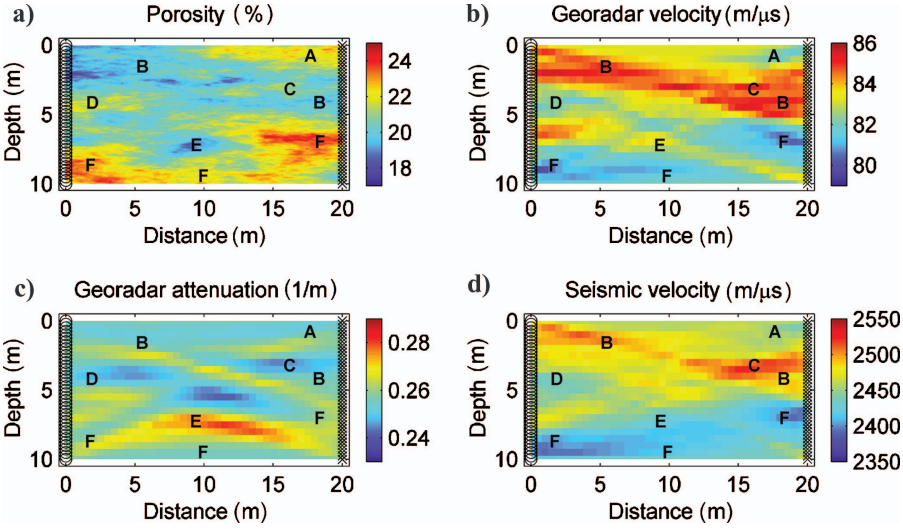

Figure 2. (a) Porosity model of a heterogeneous sedimentary aquifer. (b)–(d) Corresponding georadar velocity, georadar attenuation, and seismic P-wave velocity tomograms, respectively. Small circles and crosses along the left and right model edges delineate source and receiver locations within the boreholes, respectively. Zones A–F are explained in the text.

SYNTHETIC STUDY

Integration of physical-property models

Figure 2 shows the input porosity model and the georadar velocity and attenuation and P-wave velocity tomograms derived from inverting the corresponding synthetic data. A comparison of Figure 2b and d with Figure 2a demonstrates that the derived georadar and seismic velocities correlate approximately inversely with the porosity variations at scales larger than 1–2 m. This is particularly clear for zones A, B, D, E, and F in Figure 2a. For our synthetic model, the histographic crossplot of Figure 3a suggests an approximately linear relationship between the georadar and seismic velocities.

The relationships between the derived georadar attenuations and the porosities (Figure 2c and a) and between the derived georadar attenuations and both velocity fields (Figure 3b and c) are not so obvious. This complexity is likely the result of scattering effects within the highly heterogeneous media that are not accounted for in ray-based crosshole georadar attenuation tomography (Holliger and Maurer, 2004) and the strongly nonlinear relationship between electrical resistivity and porosity (equation 4); it is worth mentioning that the correlation between georadar attenuation (Figure 2c) and the electrical resistivity distribution (not shown) derived directly from Figure 2a using equation 4 is quite good. Despite its inherent limitations, recent studies indicate that crosshole georadar attenuation tomography can be a useful complementary tool for characterizing the shallow subsurface (Chen et al., 2001; Hubbard et al., 2001; Tronicke et al., 2004; Musil et al., 2006).

We subject the tomograms presented in Figure 2 to FCM cluster analyses assuming the presence of two, three, or four clusters. To avoid scaling effects, all tomographic results are normalized to have a mean value of zero and a standard deviation of one prior to the cluster analyses. Figure 4 shows the membership functions resulting from the three-cluster solution. Red indicates high member-

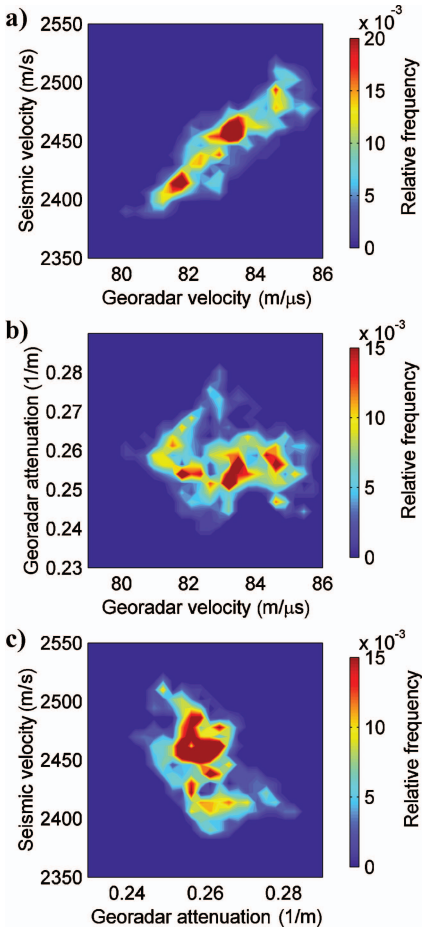

Figure 3. Colored histographic plots illustrating the relationships between (a) georadar velocity and seismic P-wave velocity, (b) georadar velocity and attenuation, and (c) georadar attenuation and seismic P-wave velocity. Relative frequency equals frequency of values divided by total number of values. See corresponding tomograms in Figure 2.

ship values (i.e., values that are close to the corresponding cluster centers), whereas blue and green indicate low to very low membership values. Figure 5 shows the hard cluster versions of the models for two-, three-, and four-cluster solutions, such that each point in the subsurface is represented by the cluster for which it has the highest membership value. In these models, each cluster represents a specific zone characterized by a distinct range of physical properties. The color saturations are proportional to the membership values. Dark colors indicate membership values close to unity, whereas pale colors represent membership values close to the lowest possible (i.e., the reciprocals of the number of clusters).

In effect, color saturation is a measure of the uniformity or heterogeneity of the zonations. By comparing the three-cluster model in Figure 5b to the initial porosity model in Figure 2a, we can readily identify clusters 1, 2, and 3 as areas of low, high, and intermediate porosity, respectively.

One fundamental drawback of all clustering techniques is that the choice of the optimum number of clusters is inherently subjective (Bezdek, 1981). Typically, this choice is guided by (1) statistical measures such as normalized classification entropy (NCE), which describes the degree of disorder present in a system (Bezdek, 1981), (2) careful analyses of the resolution of the input data, and/or (3) comparisons of the solutions for varying numbers of clusters with prior information. Our choice of the number of clusters is largely guided by these criteria. In doing so, we use the definition of Roubens (1982) for NCE:

$$\mathrm{NCE} = \frac{-\frac{1}{n} \times \sum_{i=1}^{c} \sum_{j=1}^{n} md_{ij} \times \log(md_{ij})}{\log(c)} \tag{7}$$

where $md_{ij} \times \log(md_{ij})$ is defined to equal zero when $md_{ij} = 0$ and, again, c is the number of clusters and n is the number of data points. Values of NCE vary from zero for clusters that are completely separated to one for clusters that completely overlap (i.e., cannot be separated). Tests based on synthetic clusters with varying degrees of overlap suggest that reasonably good cluster separation can be achieved when NCE values are less than 0.8 (Roubens, 1982). The NCE values obtained for the two-, three-, and four-cluster solutions shown in Figure 5 are 0.61, 0.62, and 0.61, respectively, suggesting that all solutions are adequate for our synthetic data set.

Petrophysical parameter estimation

We now attempt to reconstruct the initial 2D porosity model based on the petrophysical parameter estimation scheme outlined on the right side of Figure 1. For this purpose, we use the porosity values within the boreholes along the edges of the model shown in

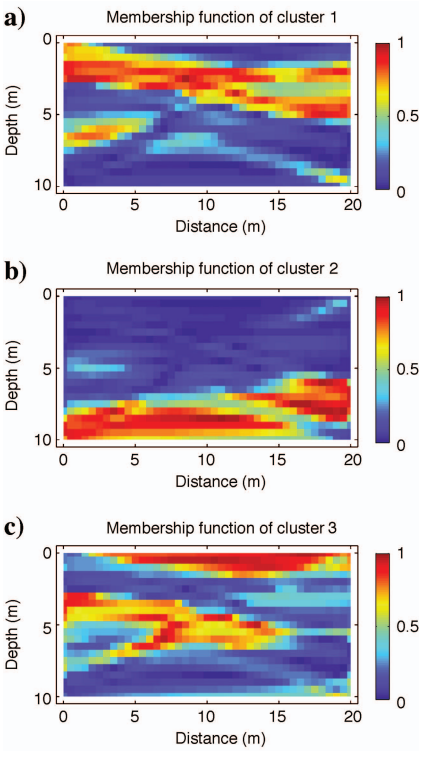

Figure 4. Membership functions for (a) cluster 1, (b) cluster 2, and (c) cluster 3 resulting from the FCM cluster analysis using a three-cluster solution for the synthetic data set of Figures 2 and 3. Summation of (a), (b), and (c) yields a value of one at each data point.

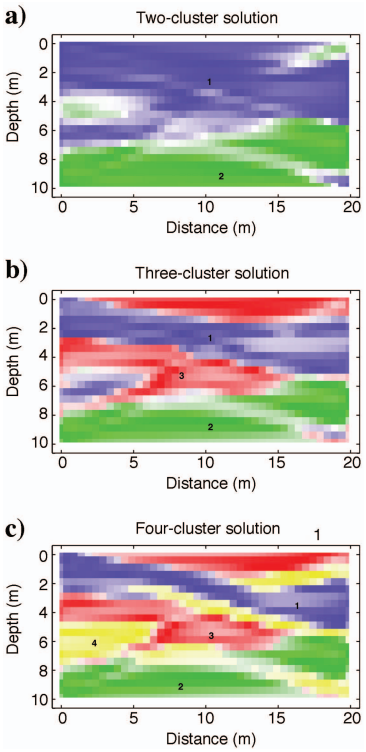

Figure 5. Zonations obtained from the synthetic data of Figures 2 and 3 for (a) two-, (b) three-, and (c) four-cluster solutions. Numbers identify the individual clusters. The primary colors represent cluster memberships after conversion to equivalent hard cluster models, whereas the color saturations indicate membership values (e.g., high color saturation indicates a high value of the corresponding membership function).

Figure 2a. Figure 6 shows crossplots of these porosity data with the corresponding membership values for the two-, three-, and four-cluster solutions. We assign to each cluster the corresponding median porosity determined from Figure 6; for these estimates, we consider only data points with membership values greater than 80% of the maximum value of the respective clusters (e.g., if the maximum membership value in any cluster is 0.9, then the 80% line is drawn at 0.72). Based on these estimates, the 2D porosity distribution is then reconstructed using equation 2.

Figure 7 shows values of the input porosity model plotted on the same 0.25-m grid used for the tomographic inversions together with the porosity distributions reconstructed from the two-, three-, and four-cluster solutions. Overall, the reconstructed porosity models are very similar to the input model, regardless of the number of clusters considered. Other computations demonstrate that the results are not greatly dependent on the choice of the threshold used to determine the median porosities of each cluster (i.e., values varying from 60%–90% yielded similarly good results).

For the different FCM analyses, the correlation coefficients and percent mean differences between the original and reconstructed porosity models range from 0.70–0.72 and from 3.08%–3.24% (Table 2), respectively. Moreover, the average porosities and standard deviations of all reconstructed models are very close to those of the input model (Table 3).

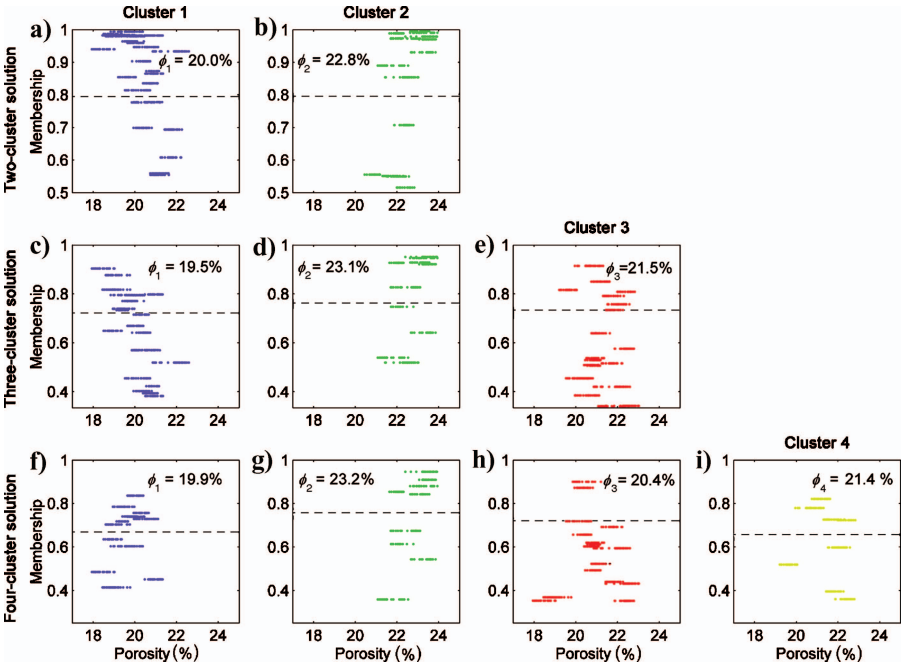

Figure 6. Relationships between porosities (Figure 2a) and FCM membership functions (e.g., Figure 4) along the two boreholes. (a)–(b) Two-cluster solution. (c)–(e) Three-cluster solution. (f)–(i) Four-cluster solution. Values above the dashed lines have membership values that are greater than 80% of the maximum membership values for the respective clusters, and the numerical values are the respective median porosities ϕ.

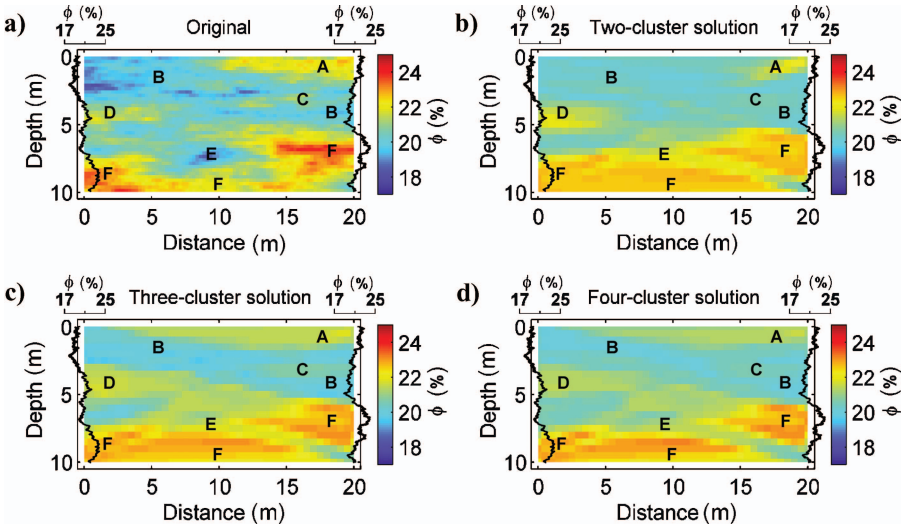

Figure 7. (a) Input porosity model (Figure 2a) resampled to allow meaningful comparisons with the other diagrams in the figure and reconstructed porosity distributions derived from (b) two-cluster, (c) three-cluster, and (d) four-cluster solutions (see Figures 4 and 5 and Tables 2 and 3). Synthetic logs extracted from the original porosity field (Figure 2a), which are used for the reconstructions, are also displayed.

FIELD STUDY

In the following section, we apply the physical-property model integration and petrophysical parameter estimation approaches to investigate a well-studied alluvial aquifer at the Kappelen test site in western Switzerland (Figure 8a and b; Kennedy et al., 2001; Flynn et al., 2004). This site is located in a forested area of the former Alte Aare River floodplain.

We collected crosshole georadar and seismic data below the groundwater table in two nearly perpendicular tomographic planes (Figure 8c). The four 15-m-deep boreholes were separated by about 20 m. Drilling reports indicated that a 1-m-thick humus layer was underlain by approximately 14 m of fluvial gravels and sands followed by silty and clayey fine sands that acted as an aquitard (Figure 8d). At the time of our surveys, the groundwater table was at roughly 4 m depth.

The crosshole georadar data were acquired with a 100-MHz antenna system. For the crosshole seismic data we used a sparker source and hydrophone receivers. The source and receiver spacings were uniformly 0.5 m for the georadar data and 0.2 and 0.25 m, respectively, for the seismic data. This resulted in approximately

1500 georadar and 7000 seismic traces. The dominant frequencies of the recorded georadar and seismic data were around 60 MHz and 700 Hz, respectively, which corresponded at this site to dominant wavelengths of 1.5 and 3 m.

Figure 9 shows typical examples of crosshole georadar and seismic data gathers, together with the semiautomatic picks of the direct-wave arrivals. Minor processing (dc-shift removal and gentle 0-15-150-200-MHz zero-phase band-pass filtering) was applied to the georadar data to enhance the reliability of the semiautomatic picking process. No processing was required for the seismic data. Based on statistical repeatabilities, the picking accuracies of the direct-wave arrivals were estimated to be around 2 ns and 0.04 ms for the georadar and seismic data, respectively. Reliable amplitude estimates were not possible in some parts of the georadar data where the direct waves interfered with critically refracted arrivals generated at the groundwater table. This limitation reduced the number of usable amplitude measurements by ~7%. Amplitudes of the direct seismic waves were not measured because more than 50% of the first arrivals were clipped.

To avoid problems associated with any minor deviations of the boreholes, we used a tomographic scheme that simultaneously inverted for velocities and borehole coordinates (Maurer, 1996; Maurer and Green, 1997). The rms differences between the predicted traveltimes based on the final tomograms and the observed georadar and seismic traveltimes were less than 2 ns and 0.05 ms, respectively, which were close to the corresponding estimated picking uncertainties.

Figure 10 shows the resulting georadar velocity and attenuation and seismic P-wave velocity tomograms for both planes. The geo-

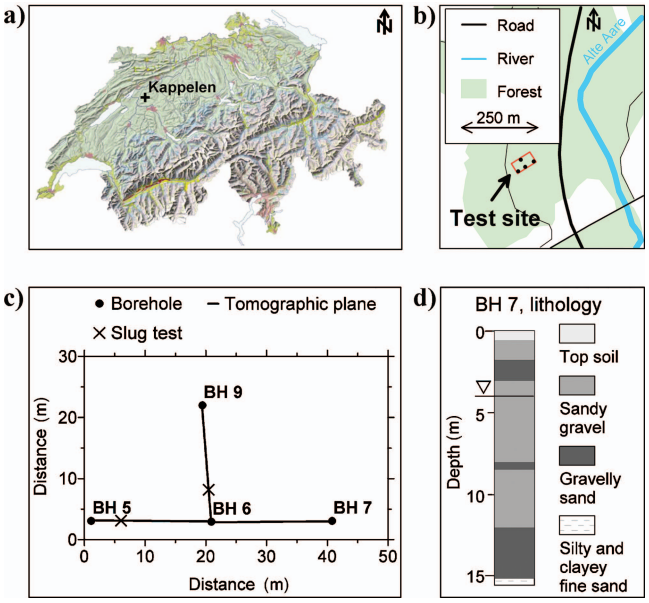

Figure 8. The Kappelen hydrological test site is located in (a) western Switzerland in (b) a forested area close to the Alte Aare River. The red box marks the area enlarged in (c). (c) Crosshole geophysical data were collected between boreholes (BH) 5, 6, and 7 and between boreholes 6 and 9. Slug tests were performed at the locations marked by crosses. (d) Typical example of a borehole litholog, showing that the probed aquifer consists predominantly of fluvial deposits.

Table 2. Correlation coefficients and mean differences of reconstructed porosity distributions with respect to the original porosity model (Figure 7).

Reconstruction	Correlation coefficients	Mean differences (%)
Two cluster	0.70	3.17
Three cluster	0.72	3.24
Four cluster	0.72	3.08

Table 3. Mean values and standard deviations of original (Figure 2a), resampled (Figure 7a), and reconstructed porosity models (Figures 7b–7d).

Model	Mean porosities (%)	Standard deviations (%)
Original (Figure 2a)	21.0	1.1
Resampled (Figure 7a)	21.0	1.1
Two-cluster reconstruction (Figure 7b)	21.2	1.0
Three-cluster reconstruction (Figure 7c)	21.3	1.0
Four-cluster reconstruction (Figure 7d)	21.2	1.0

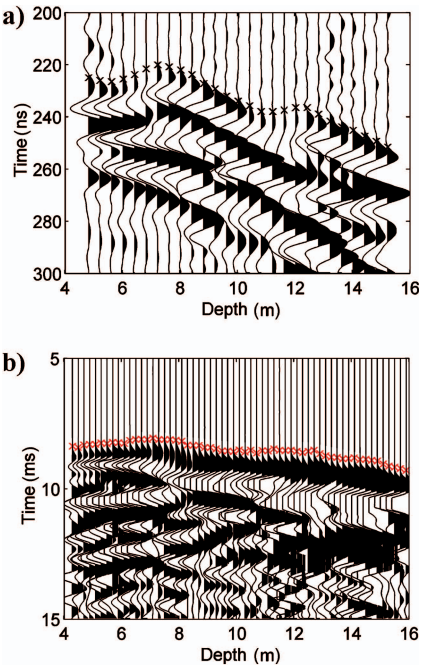

Figure 9. Typical crosshole data gathers observed in the tomographic plane between boreholes 6 and 9. (a) Georadar source gather after minor processing (transmitter at 6.98-m depth in borehole 6) and (b) raw seismic receiver gather (receiver at 6.9-m depth in borehole 6). Crosses show the picked first arrivals. The coherent energy arriving prior to the direct wave on the shallow traces in (a) was refracted at the groundwater table.

radar and seismic velocity tomograms (Figure 10a, b, e, and f) are similar to each other. They indicate the subsurface is quasi-layered with a subhorizontal zone characterized by low georadar and low seismic velocities at 7–12 m depth. The thickness of this low-velocity zone increases toward borehole 9. As for our synthetic study, the georadar attenuation pattern differs somewhat from the georadar and seismic velocity patterns.

Integration of physical-property models

Histographic crossplots in Figure 11 illustrate the interrelationships of the tomographically determined parameters. We use FCM to integrate the tomographic images represented in Figures 10 and 11 assuming two, three, and four clusters. As an example, Figure 12 shows the membership functions for the three-cluster solution. The corresponding hard cluster versions of the two-, three-, and four-cluster models are shown in Figure 13. The mean values and standard deviations of the various clusters are given in Table 4. Although all models in Figure 13 are approximately horizontally layered, there are significant lateral variations.

The NCE values for the two-, three-, and four-cluster solutions are 0.74, 0.75, and 0.75, respectively. Based on these results and accounting for the resolution of the geophysical data, the two- and three-cluster solutions appear to be adequate. Cluster 1 in the two- and three-cluster solutions outlines the same general subsurface regions distinguished by low georadar and low seismic velocities (Figures 10, 12, and 13). In contrast, cluster 2 in the two-cluster solution is represented in the three-cluster solution by clusters 2 and 3, which differ primarily in their georadar attenuation values (Table 4).

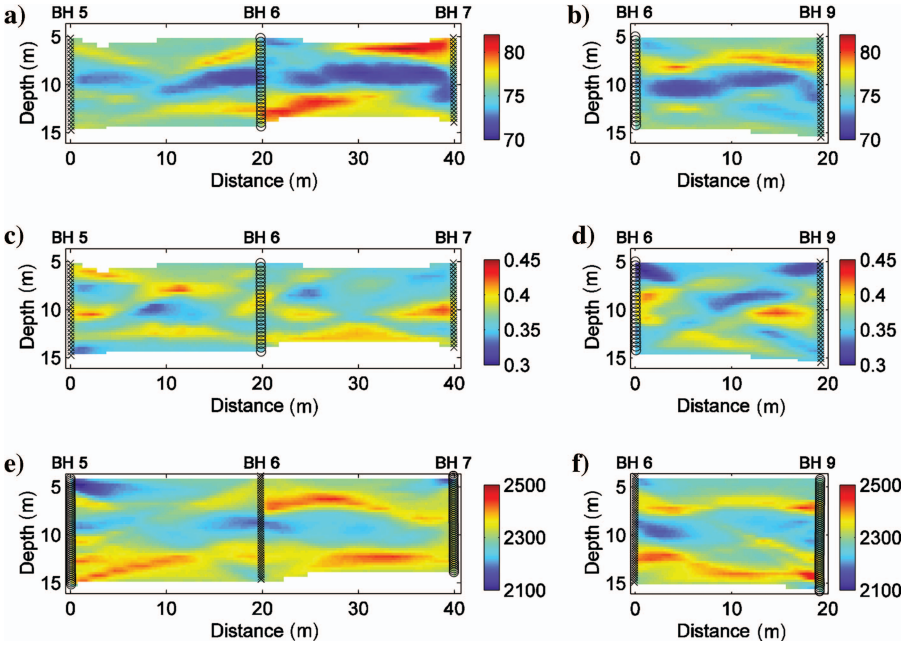

Figure 10. Results of tomographic inversions of the Kappelen crosshole data. Georadar velocity tomograms for borehole planes (a) 5-6-7 and (b) 6-9. Georadar attenuation tomograms for borehole planes (c) 5-6-7 and (d) 6-9. Seismic P-wave velocity tomograms for borehole planes (a) 5-6-7 and (b) 6-9. Circles and crosses along the boreholes delineate source and receiver locations, respectively.

Petrophysical parameter estimation

Natural gamma logs and the results of direct-push slug tests (Butler et al., 2000) provided our most reliable petrophysical data at the Kappelen test site. Variations in natural gamma-ray activity in counts per second (cps), widely regarded as a proxy for lithological variations (Cripps and McCann, 2000), were measured at 0.05-m intervals along the boreholes (Figure 8c) using a standard commercial logging tool. Hydraulic conductivities were estimated on the basis of nine slug tests performed with a direct-push device. Eight slug tests with a vertical spacing of 1 m were completed about 5 m to the east of borehole 5, covering a depth range from approximately 5.8–12.8 m (Figure 8c). An additional single slug test was carried out in the plane between boreholes 6 and 9, approximately 5 m to the north of borehole 6 at a depth of about 12.3 m (Figure 8c).

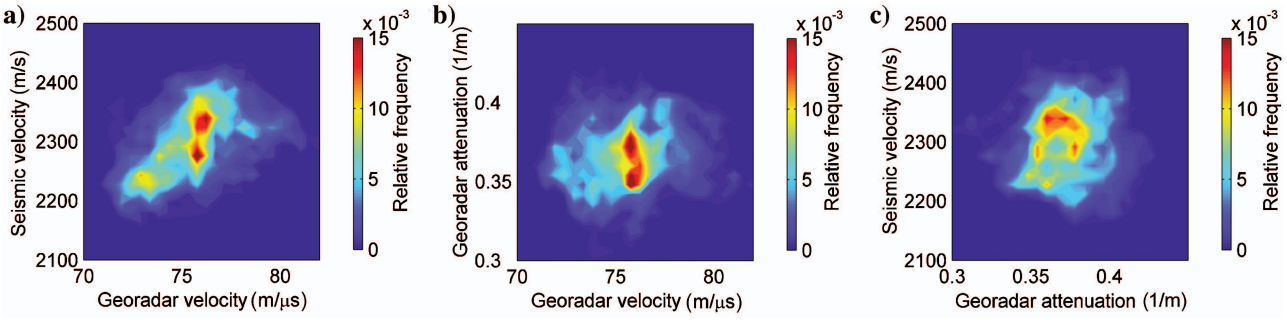

Figure 11. For the tomograms displayed in Figure 10, the colored histographic plots illustrate the relationships between the tomographically derived (a) georadar velocity and seismic P-wave velocity, (b) georadar velocity and georadar attenuation, and (c) georadar attenuation and seismic P-wave velocity. Relative frequency equals frequency of values divided by total number of values.

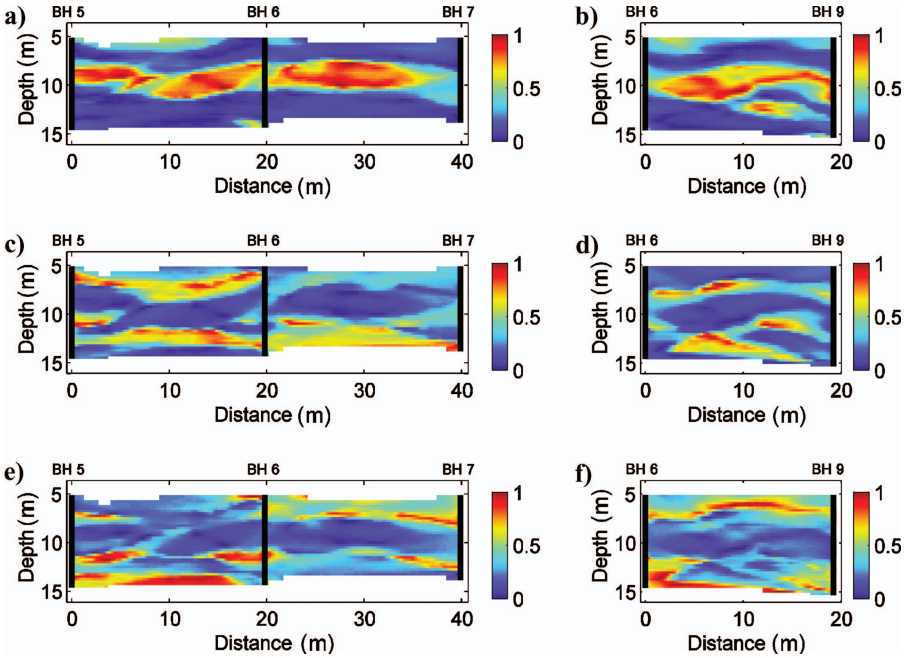

Figure 12. Membership functions resulting from the FCM cluster analysis using a three-cluster solution for the tomograms shown in Figure 10.

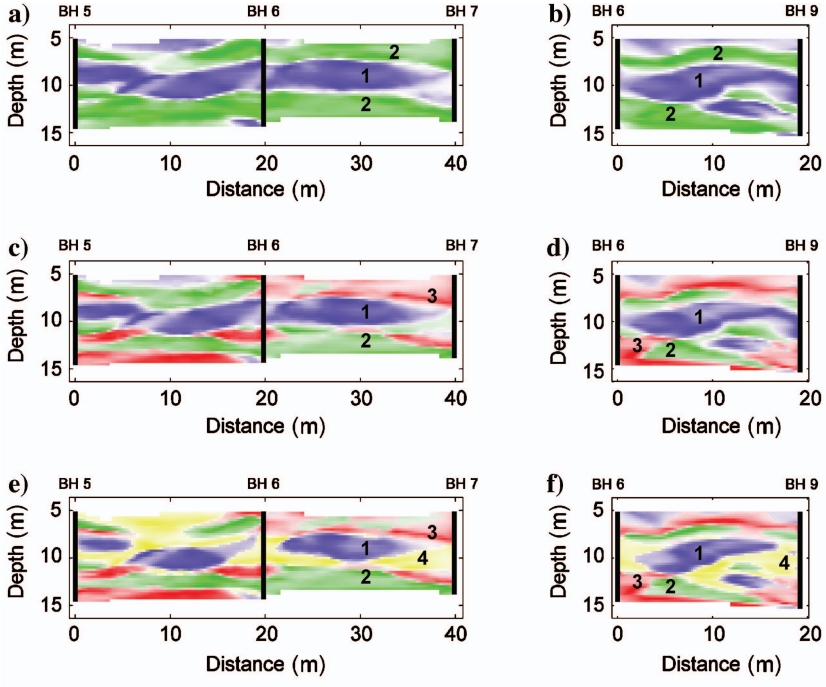

Figure 13. Zoned models of the probed subsurface region for (a)–(b) two-, (c)–(d) three-, and (e)–(f) four-cluster solutions. Numbers identify the individual clusters. The primary colors denote memberships to the various clusters after conversion to hard cluster models, whereas the color saturations indicate the membership values (e.g., high color saturation indicates a high value of the corresponding membership function).

Figure 14 shows gamma-ray logs and hydraulic conductivities together with the extrapolated distributions of gamma-ray activity and hydraulic conductivity based on the three-cluster solution of Figure 13c and d. To determine the distribution of gamma-ray activity, we only use gamma-log data from boreholes 5, 6, and 7, thus allowing the data from borehole 9 to be used as a test of the petrophysical parameter estimation procedure (see below). It is noteworthy that the 7.0–8.5 cps and $10^{-2.9}$ to $10^{-3.7}$ m/s ranges of extrapolated gamma-ray and hydraulic conductivity values are significantly lower than the corresponding 5–10 cps and $10^{-2.9}$ to $10^{-5.0}$ m/s ranges of the observed values. This phenomenon is attributable to a combination of effects, including the limited resolution of the crosshole seismic and georadar data sets, the inherent smoothing and damping of the ray-based tomographic inversion procedure, and the averaging involved in the reconstruction process (equation 2; Day-Lewis and Lane, 2004; Moysey et al., 2005).

Figure 15a compares the extrapolated gamma-ray activity at borehole 9 (blue line) to that recorded in the borehole (black line). To compensate for its lower dynamic range, we also show the extrapolated gamma-ray activity adjusted to have the same standard deviation as the measured curve (red line). Clearly, our FCM cluster technique cannot predict the short-wavelength undulations of the recorded data, but the long-wavelength trend of recorded values is reasonably well represented by the extrapolated gamma-ray activity.

We do not have sufficient data to test thoroughly the extrapolations of the hydraulic conductivity estimates. Nevertheless, with the exception of the estimate at about 7 m depth, the results shown in Figure 15b demonstrate that the general trend of the extrapolated hydraulic conductivities is compatible with the observed values on which they are partially based.

Despite the rather limited database, the nearly coincident zones of relatively high gamma-ray activity and high hydraulic conductivity suggest that the fluvial gravels and sands between 1- and 14-m depth are to a first order horizontally continuous, but that significant vertical and horizontal heterogeneity exists. This assertion is consistent with information extracted

Table 4. Mean values and standard deviations for the various clusters shown in Figure 13.

Model	Cluster number	Georadar velocities ($m/\mu s$)	Georadar attenuations (1/m)	P-Wave velocities (m/s)
Two-cluster solution (Figure 14a and b)	1	73.8 ± 1.3	0.364 ± 0.020	2264 ± 37
	2	76.5 ± 1.5	0.373 ± 0.017	2345 ± 38
Three-cluster solution (Figure 14c and d)	1	73.4 ± 1.2	0.364 ± 0.018	2252 ± 31
	2	76.4 ± 1.6	0.387 ± 0.012	2329 ± 45
	3	75.9 ± 1.6	0.357 ± 0.012	2341 ± 38
Four-cluster solution (Figure 14e and f)	1	73.3 ± 1.2	0.352 ± 0.014	2255 ± 32
	2	77.2 ± 1.4	0.383 ± 0.012	2352 ± 36
	3	75.8 ± 1.4	0.357 ± 0.010	2344 ± 35
	4	74.4 ± 1.3	0.385 ± 0.013	2269 ± 36

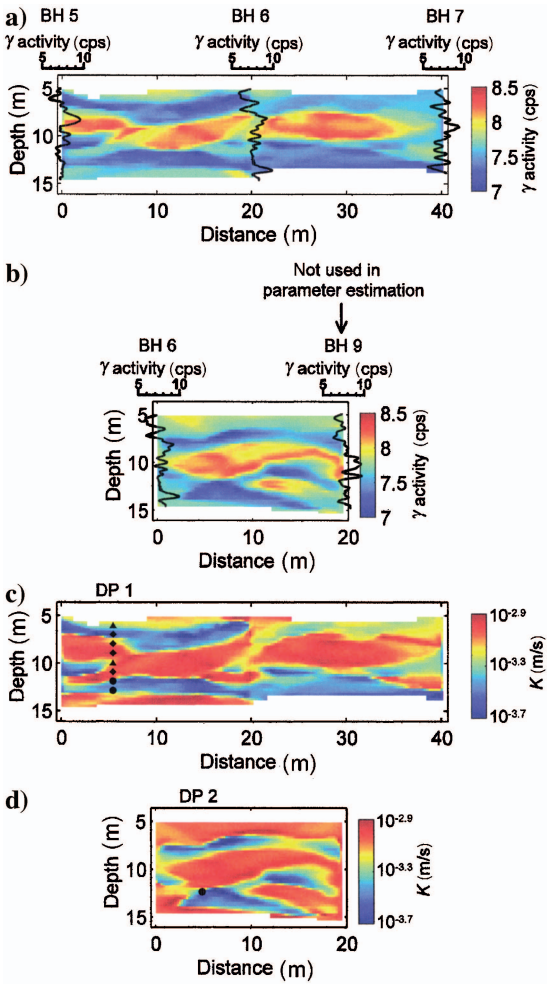

Figure 14. For the Kappelen test site, estimates of the spatial distributions of (a)–(b) gamma-ray activity and (c)–(d) hydraulic conductivity based on the three-cluster solution (Figures 13c and 13d) and corresponding natural gamma-log and direct-push (DP) slug-test data. Only the gamma-ray logs from boreholes 5, 6, and 7 were used to constrain the spatial distributions of gamma-ray activity. The gamma-ray log from borehole 9 was used to test the results (see Figure 15a). In (c) and (d), diamonds, triangles, and dots represent hydraulic conductivities greater than $10^{-3.4}$, from $10^{-3.4}$ to $10^{-4.0}$, and less than $10^{-4.0}$ m/s, respectively.

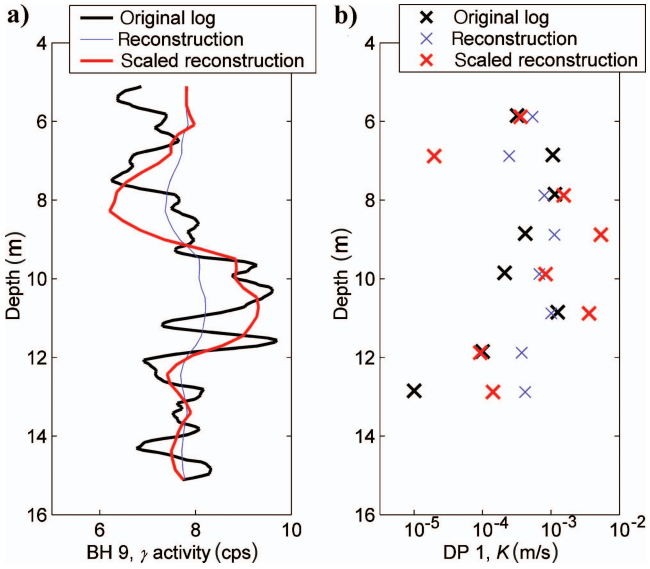

Figure 15. (a) Comparison of extrapolated gamma-ray activity (blue and red lines) with values measured in borehole 9 (black line). The extrapolated gamma-ray activity represented by the red line has been scaled to have the same standard deviation as the measured data represented by the black line (see text for the reasons for this processing step). (b) Comparison of extrapolated hydraulic conductivities (blue and red crosses) with direct-push slug-test measurements (black crosses). The extrapolated hydraulic conductivities represented by the red crosses are scaled to have the same standard deviation as the measured data represented by the black crosses (see text for the reasons for this processing step).

from a large number of boreholes at the Kappelen test site (R. Flynn, personal communication, 2005).

CONCLUSIONS

We explore the utility of the FCM clustering technique for combining information contained in different physical-property models to form a single zoned multiparameter model and for estimating the spatial distribution of petrophysical parameters from limited geophysical and petrophysical databases. FCM cluster analysis enables us to identify and map zones characterized by similar or consistent relationships between the estimated physical properties. Membership functions, which provide quantitative information on the similarity of data that define the clusters, allow us to assess the uniformity or heterogeneity of the clusters. One drawback of most clustering techniques is the absence of robust criteria for determining the optimum number of clusters for a given investigation. This problem can be alleviated by (1) using statistical cluster validation criteria, (2) considering the resolution of the various data sets, and/or (3) comparing the various solutions obtained using different numbers of clusters with complementary geological, hydrological, and geophysical information.

An important outcome of this study is the development of a method for estimating the spatial distribution of petrophysical parameters (e.g., lithologies, porosities, and hydraulic conductivities) that cannot be determined uniquely from the physical-property models or geophysical data. The petrophysical parameters of interest must only be known at a limited number of locations within the probed subsurface volume — for example, along boreholes. To ensure meaningful estimates of the spatial distribution of petrophysi-

cal parameters, they must be correlated, albeit imperfectly, to the physical properties used to determine the zonations. It is important to emphasize that the nature of these interrelations does not need to be known or specified explicitly. Our tests on synthetic and field data suggest that within the resolution of the recorded geophysical data, the estimated petrophysical parameter distributions are realistic; most importantly, their overall quality is not strongly dependent on the number of predefined clusters. A major advantage of this petrophysical parameter estimation approach lies in the quantitative integration of multiple physical-property models, whereas more traditional approaches based on empirical or semiempirical expressions usually only relate individual petrophysical parameters to individual physical properties (e.g., equations 3–6). The model integration and parameter estimation approach described in this paper may be applicable to a wide range of 2D and 3D geophysical data and techniques.

ACKNOWLEDGMENTS

We thank R. Flynn (University of Neuchâtel, Switzerland) for giving us access to the Kappelen field site and providing essential background information. We also thank the GEOPHYSICS editors and reviewers for their constructive comments. The research was funded by the Swiss National Science Foundation.

REFERENCES

Aaltonen, J., 2003, The combination of GPR and CVES measurements: Near Surface Geophysics, **1**, 197–201.

Archie, G. E., 1942, The electrical resistivity log as an aid in determining some reservoir characteristics: Transactions of the American Institute of Mining, Metallurgical and Petroleum Engineers, **146**, 54–62.

Bergmann, T., J. O. Robertsson, and K. Holliger, 1996, Numerical properties of staggered finite-difference solutions of Maxwell's equations for ground-penetrating radar modeling: Geophysical Research Letters, **23**, 45–48.

Bezdek, J. C., 1981, Pattern recognition with fuzzy objective function algorithms: Plenum Press.

Bosch, M., 2004, The optimization approach to lithological tomography: Combining seismic data and petrophysics for porosity prediction: Geophysics, **69**, 1272–1282.

Bragato, G., 2004, Fuzzy continuous classification and spatial interpolation in conventional soil survey for soil mapping of the lower Piave plain: Geoderma, **118**, 1–16.

Butler, J. J., A. A. Lanier, J. M. Healey, S. M. Sellwood, W. McCall, and E. Garnett, 2000, Direct-push hydraulic profiling in an unconsolidated alluvial aquifer: Kansas Geological Survey Open-File Report 2000–62.

Chen, J., S. Hubbard, and Y. Rubin, 2001, Estimating hydraulic conductivity at the South Oyster site from geophysical tomographic data using Bayesian techniques based on the normal regression model: Water Resources Research, **37**, 1603–1613.

Cripps, A. C., and D. M. McCann, 2000, The use of the natural gamma log in engineering geological investigations: Engineering Geology, **5**, 313–324.

Dannowski, G., and U. Yaramanci, 1999, Estimation of water content and porosity using combined radar and geoelectrical measurements: European Journal of Environmental and Engineering Geophysics, **4**, 71–85.

Day-Lewis, F. D., and J. W. Lane, 2004, Assessing the resolution-dependent utility of tomograms for geostatistics: Geophysical Research Letters, **31**, L07503, doi:10.1029/2004GL019617.

De Bruin, S., and A. Stein, 1998, Soil-landscape modelling using fuzzy *c*-means clustering of attribute data derived from a digital elevation model (DEM): Geoderma, **83**, 17–33.

Desbarats, A. J., and S. Bachu, 1994, Geostatistical analysis of aquifer heterogeneity from the core to the basin scale: A case study: Water Resources Research, **30**, 673–684.

Dietrich, P., T. Fechner, J. Whittacker, and G. Teutsch, 1998, An integrated hydrogeophysical approach to subsurface characterization: International Association of Hydrological Sciences Publication, **250**, 513–519.

Ernst, J. R., K. Holliger, H. Maurer, and A. G. Green, 2006, Realistic FDTD modelling of borehole georadar antenna radiation: Methodology and application: Near Surface Geophysics, **4**, 19–30.

Flynn, R., D. Hunkeler, C. Guerin, C. Burn, P. Rossi, and M. Aragno, 2004, Geochemical influences on H40/1 bacteriophage inactivation in glaciofluvial sands: Geophysics, **45**, 504–517.

Fridgen, J. J., N. R. Kitchen, K. A. Sudduth, S. T. Drummond, W. J. Wiebold, and C. W. Fraisse, 2004, Management zone analyst (MZA): Software for subfield management zone delineation: Agronomy Journal, **96**, 100–108.

Fuchs, K., and G. Müller, 1971, Computation of synthetic seismograms with the reflectivity method and comparison with observations: Geophysical Journal of the Royal Astronomical Society, **23**, 417–433.

Gaffney, V., H. Patterson, S. Piro, D. Goodman, and Y. Nishimura, 2004, Multimethodological approach to study and characterize Forum Novum (Vescovio, central Italy): Archeological Prospection, **11**, 201–212.

Gallardo, L. A., and M. A. Meju, 2003, Characterization of heterogeneous near-surface materials by joint 2D inversion of dc resistivity and seismic data: Geophysical Research Letters, **30**, doi: 10.1029/2003GL017370.

Garambois, S., P. Sénéchal, and H. Perroud, 2002, On the use of combined geophysical methods to assess water content and water conductivity of near-surface formations: Journal of Hydrology, **259**, 32–48.

Gelhar, L. W., 1993, Stochastic subsurface hydrology: Prentice-Hall, Inc.

Goff, J. A., and T. H. Jordan, 1988, Stochastic modeling of seafloor morphology: Inversion of sea beam data for second-order statistics: Journal of Geophysical Research, **93**, 13589–13608.

Greaves, R. J., D. P. Lesmes, J. M. Lee, and M. N. Toksöz, 1996, Velocity variations and water content estimated from multioffset, ground-penetrating radar: Geophysics, **61**, 683–695.

Güler, C., and G. D. Thyne, 2004, Delineation of hydrochemical facies distribution in a regional groundwater system by means of fuzzy *c*-means clustering: Water Resources Research, **40**, doi 10.1029/2004WR003299.

Hardy, H. H., and R. A. Beier, 1994, Fractals in reservoir engineering: World Scientific.

Hathaway, R. J., and J. C. Bezdek, 2001, Fuzzy *c*-means clustering of incomplete data: IEEE Transactions on Systems, Man, and Cybernetics, Part B: Cybernetics, **31**, 735–744.

Heinz, J., S. Kleineidam, G. Teutsch, and T. Aigner, 2003, Heterogeneity patterns of Quaternary glaciofluvial gravel bodies (SW Germany): Application to hydrology: Geophysics, **158**, 1–23.

Holliger, K., and T. Bergmann, 2002, Numerical modeling of borehole georadar data: Geophysics, **67**, 1249–1257.

Holliger, K., and H. R. Maurer, 2004, Effects of stochastic heterogeneity on ray-based tomographic inversion of crosshole georadar amplitude data: Journal of Applied Geophysics, **56**, 177–193.

Holliger, K., M. Musil, and H. R. Maurer, 2001, Ray-based amplitude tomography for crosshole georadar data: A numerical assessment: Journal of Applied Geophysics, **47**, 285–298.

Höppner, F., F. Klawonn, R. Kruse, and T. Runkler, 1999, Fuzzy cluster analysis: Methods for classification, data analysis and image recognition: John Wiley & Sons, Inc.

Hubbard, S. S., J. Chen, J. E. Peterson, E. L. Majer, K. H. Williams, D. J. Swift, B. Mailloux, and Y. Rubin, 2001, Hydrogeological characterization of the South Oyster bacterial transport site using geophysical data: Water Resources Research, **37**, 2431–2456.

Kaufmann, L., and P. J. Rousseeuw, 1990, Finding groups in data: An introduction to cluster analysis: John Wiley & Sons, Inc.

Kennedy, K., I. Müller, P. Schnegg, P. Rossi, and R. Koezel, 2001, Characterisation of the Kappelen groundwater research site (BE), Switzerland and preliminary bacteriophage and solute tracer component responses: Beiträge zur Hydrogeologie, **52**, 158–180.

Knab, M., E. Appel, and V. Hoffmann, 2001, Separation of the anthropogenic portion of heavy metal contents along a highway by means of magnetic susceptibility and fuzzy *c*-means cluster analysis: European Journal of Environmental and Engineering Geophysics, **6**, 125–140.

Kostyuchenko, S. L., A. F. Morozov, R. A. Stephenson, L. N. Solodilov, A. G. Vedrentsev, K. E. Popolitov, A. F. Aleshina, V. S. Vishnevskaya, and T. P. Yegorova, 2004, The evolution of the southern margin of the East European Craton based on seismic and potential field data: Tectonophysics, **381**, 101–118.

Kruiver, P. P., Y. S. Kok, M. J. Dekkers, C. G. Langereis, and C. Laj, 1999, A pseudo-Thellier relative palaeointensity record, and rock magnetic and geochemical parameters in relation to climate during the last 276 kyr in the Azores region: Geophysical Journal International, **136**, 757–770.

Küpper, F. J., 1958, Theoretische Untersuchungen über die Mehrfachaufstellung von Geophonen: Geophysical Prospecting, **6**, 194–254.

Lampe, B., and K. Holliger, 2005, Resistively loaded antennas for ground-penetrating radar: A modeling approach: Geophysics, **70**, K23–K32.

Lanz, E., H. R. Maurer, and A. G. Green, 1998, Refraction tomography over a buried waste disposal site: Geophysics, **63**, 1414–1433.

Maurer, H. R., 1996, Systematic errors in seismic crosshole data: Application of the coupled inverse technique: Geophysical Research Letters, **23**, 2681–2684.

Maurer, H. R., and A. G. Green, 1997, Potential coordinate mislocations in crosshole tomography: Results from the Grimsel test site, Switzerland:

Geophysics, **62**, 1696–1709.
Melgani, F., B. A. R. Al Hasemy, and S. M. R. Taha, 2000, An explicit fuzzy supervised classification method for multispectral remote sensing images: IEEE Transactions on Geoscience and Remote Sensing, **38**, 287–295.
Moysey, S., K. Singha, and R. Knight, 2005, A framework for inferring field-scale rock physics relationships through numerical simulation: Geophysical Research Letters, **32**, L08304 doi:10.1029/2004GL022152.
Musil, M., H. R. Maurer, and A. G. Green, 2003, Discrete tomography and joint inversion for loosely connected or unconnected physical properties: Application to crosshole seismic and georadar data sets: Geophysical Journal International, **153**, 389–402.
Musil, M., H. Maurer, K. Hollinger, and A. G. Green, 2006, Internal structure of an Alpine rock glacier based on crosshole georadar traveltimes and amplitudes: Geophysical Prospecting, **54**, 273–285.
Raymer, L. L., E. R. Hunt, and J. S. Gardner, 1980, An improved sonic transit time-to-porosity transform: 21st Annual Symposium, Society of Professional Well Log Analysts, Transactions, Paper P.
Roubens, M., 1982, Fuzzy clustering algorithms and their cluster validity: European Journal of Operational Research, **10**, 294–301.
Schön, J. H., 1998, Physical properties of rocks: Fundamentals and principles of petrophysics: Pergamon Press, Inc.
Tronicke, J., N. Blindow, R. Gross, and M. A. Lange, 1999, Joint application of surface electrical resistivity- and GPR-measurements for groundwater exploration on the island of Spiekeroog — northern Germany: Journal of Hydrology, **223**, 44–53.
Tronicke, J., and K. Holliger, 2005, Quantitative integration of hydrogeophysical data: Conditional geostatistical simulation for characterizing heterogeneous alluvial aquifers: Geophysics, **70**, H1–H10.
Tronicke, J., K. Holliger, W. Barrash, and M. D. Knoll, 2004, Multivariate analysis of cross-hole georadar velocity and attenuation tomograms for aquifer zonation: Water Resources Research, **40**, doi:10.1029/2003WR 002031.
Urbat, M., M. J. Dekkers, and K. Krumsiek, 2000, Discharge of hydrothermal fluids through sediment at the Escanaba Trough, Gorda Ridge (ODP Leg 169): Assessing the effects on the rock magnetic signal: Earth and Planetary Science Letters, **176**, 481–494.
Vozoff, K., and D. L. B. Jupp, 1975, Joint inversion of geophysical data: Geophysical Journal of the Royal Astronomical Society, **42**, 977–991.
Wharton, R. P., G. A. Hazen, R. N. Rau, and D. L. Best, 1980, Advancements in electromagnetic propagation logging: 55th Annual Fall Technical Conference, SPE-AIME, Proceedings, SPE 9267.
Yaramanci, U., G. Lange, and M. Hertrich, 2002, Aquifer characterisation using surface NMR jointly with other geophysical techniques at the Nauen/Berlin test site: Journal of Applied Geophysics, **50**, 47–65.